POLITECNICO DI TORINO
Repository ISTITUZIONALE

Granular-front formation in free-surface flow of concentrated suspensions

*Original*
Granular-front formation in free-surface flow of concentrated suspensions / Leonardi, A., Cabrera, M., Wittel, F.K., Kaitna, R., Mendoza, M., Wu, W., Herrmann, H.J.. - In: PHYSICAL REVIEW E, STATISTICAL, NONLINEAR, AND SOFT MATTER PHYSICS. - ISSN 1539-3755. - 92:5(2015), p. 052204. [10.1103/PhysRevE.92.052204]

*Availability:*
This version is available at: 11583/2713374 since: 2018-09-19T17:16:55Z

*Publisher:*
American Physical Society

*Published*
DOI:10.1103/PhysRevE.92.052204

*Terms of use:*

This article is made available under terms and conditions as specified in the corresponding bibliographic description in the repository

*Publisher copyright*

(Article begins on next page)

08 October 2026

# Granular-front formation in free-surface flow of concentrated suspensions

Alessandro Leonardi,[1,2,*] Miguel Cabrera,[3,†] Falk K. Wittel,[1] Roland Kaitna,[4] Miller Mendoza,[1] Wei Wu,[3] and Hans J. Herrmann[1]

[1]*Institute for Building Materials, ETH Zurich, Computational Physics for Engineering Materials, Stefano-Franscini-Platz 3, 8093 Zurich, Switzerland*

[2]*Itasca Consulting GmbH, Leithestrasse 111, 45886 Gelsenkirchen, Germany*

[3]*Institute of Geotechnical Engineering, University of Natural Resources and Life Sciences (BOKU), Feistmantelstrasse 4, 1180 Vienna, Austria*

[4]*Institute of Mountain Risk Engineering, University of Natural Resources and Life Science (BOKU), Peter-Jordan-Strasse 82, 1190 Vienna, Austria*

(Received 20 February 2015; revised manuscript received 23 October 2015; published 23 November 2015)

A granular front emerges whenever the free-surface flow of a concentrated suspension spontaneously alters its internal structure, exhibiting a higher concentration of particles close to its front. This is a common and yet unexplained phenomenon, which is usually believed to be the result of fluid convection in combination with particle size segregation. However, suspensions composed of uniformly sized particles also develop a granular front. Within a large rotating drum, a stationary recirculating avalanche is generated. The flowing material is a mixture of a viscoplastic fluid obtained from a kaolin-water dispersion with spherical ceramic particles denser than the fluid. The goal is to mimic the composition of many common granular-fluid materials, such as fresh concrete or debris flow. In these materials, granular and fluid phases have the natural tendency to separate due to particle settling. However, through the shearing caused by the rotation of the drum, a reorganization of the phases is induced, leading to the formation of a granular front. By tuning the particle concentration and the drum velocity, it is possible to control this phenomenon. The setting is reproduced in a numerical environment, where the fluid is solved by a lattice-Boltzmann method, and the particles are explicitly represented using the discrete element method. The simulations confirm the findings of the experiments, and provide insight into the internal mechanisms. Comparing the time scale of particle settling with the one of particle recirculation, a nondimensional number is defined, and is found to be effective in predicting the formation of a granular front.

DOI: 10.1103/PhysRevE.92.052204 PACS number(s): 45.70.Ht, 45.70.Mg, 47.57.Gc, 47.57.E−

## I. INTRODUCTION

The study of natural hazards often deals with concentrated suspension, a prominent example being the mixture of water and granular sediments that gives origin to debris flows [1]. Such flows are well known for the large amount of granular material that they are able to transport, often over very long distances and even on gentle slopes [2]. In a debris flow, the grains are denser than the fluid, and tend to settle towards the bottom of the flow. However, *in situ* observations [3–5] consistently report that the front of the flow appears to be rich in large grains and often unsaturated, a situation that led to coining the term "granular front." This is counterintuitive, since grains exhibit frictional behavior, which leads them to offer more resistance to motion than the surrounding fluid, especially down inclines that are not steeper than their natural angle of repose. This poorly understood phenomenon is common in every suspension of the same type, and similar mechanisms have also been observed in snow avalanches [6] and pyroclastic flows [7]. In these flows, the formation of granular fronts is usually explained as a consequence of grain-size segregation. However, suspensions composed of similarly sized grains are also known to exhibit the same phenomenon [8]. In this work, the conditions leading to the formation of a granular front are investigated through a combination of an experimental study and of numerical simulations.

The experiments are performed by shearing a monodisperse suspension of roughly spherical particles immersed in a yield-stress fluid (approximated as a Bingham fluid). The plasticity of the fluid is not sufficiently high to block the particles from settling in the direction of gravity, and therefore the granular phase and the fluid phase spontaneously separates even in the absence of external excitation. The material is sheared inside a large rotating drum [see Figs. 1(a), 3]. In contrast to the common practice of drum experiments [9–19], the drum is filled with very little material (less than 2% of the available volume as in Refs. [20–24]) which recirculates due to the combination of the drum revolution and of gravity. Settling induces a phase separation, and two distinct fronts can be observed: one for the fluid, located at the angular position $\theta_f$, and one for the particles, located at $\theta_p$, as shown in Fig. 1(b). In the following, we use the term "particle front" to point to the position of the first particle, while "granular front" is used whenever the first particle is located before the fluid front [see Eq. (1)].

Both fluid and particle fronts show an oscillating behavior. After activating of the drum, the oscillations quickly reduce in amplitude and stabilize around a point of equilibrium. The relative proportion between fluid and particles is chosen so that, if the drum is rotating at a low speed, the position of the particle front lies inside the fluid, i.e., $\theta_p > \theta_f$ (see Fig. 1 for the reference system). By increasing the speed of the drum, the center of volume of the flowing mass $\theta_c$ moves upwards, i.e.,

*aleonardi@ethz.ch
†miguel.cabrera@boku.ac.at

 ©2015 American Physical Society

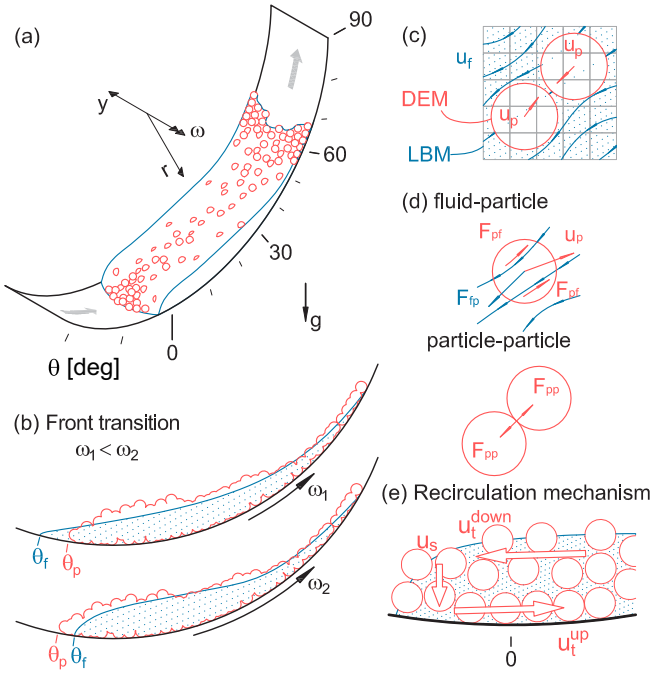


FIG. 1. (Color online) Schematics of the particle fluid mechanisms occurring in a rotating drum test. The color scheme is blue for the fluid and red for the particles. (a) Rotating drum reference system and common particle-fluid distribution. (b) Granular-front formation process by increasing the rotational velocity of the drum $\omega$. (c) LBM and DEM discretization mesh employed in the numerical simulations (a two-dimensional view is presented for simplicity). (d) Fluid-particle and particle-particle interactions considered as a result of a granular flow through a viscous flowing fluid. (e) Motion pattern of the particles at the front.

in the positive direction of $\theta$. At the same time, the two fronts get closer, the gap separating them $\Delta\theta = \theta_p - \theta_f$ becoming smaller until they eventually merge ($\Delta\theta \simeq 0$). The result is a granular front which strikingly resembles the one of a natural debris flow (see Fig. 2). In this work, we study the conditions that lead to this behavior, with focus on how $\Delta\theta$ depends on the rotational speed of the drum, $\omega$. The following terminology will be used:

$$\begin{aligned} &\Delta\theta > 0 \ \ (\theta_p > \theta_f) \rightarrow \text{fluid front}, \\ &\Delta\theta \simeq 0 \ \ (\theta_p \simeq \theta_f) \rightarrow \text{transition}, \\ &\Delta\theta < 0 \ \ (\theta_p < \theta_f) \rightarrow \text{granular front}. \end{aligned} \tag{1}$$

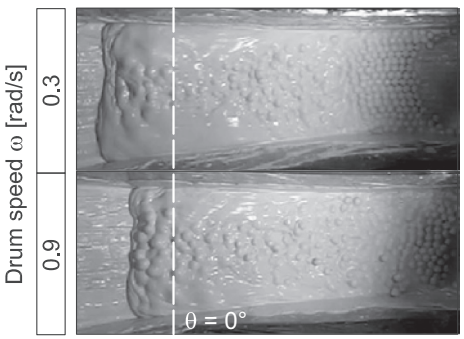


FIG. 2. Pictures of the flow inside the drum. The same material shows different features at low and high drum speed.

Experiments aiming at reproducing this phenomenon, which has been previously reported by Ref. [22], are not restricted to the drum. The granular-front formation has been addressed over the last years for the case of a thin film particle-laden flow on an incline [25–27], which more closely reproduces the actual geometry of a natural gravitational flow. In particular, the results of Murisic *et al.* [27] highlight how the formation of a granular front is induced by the equilibrium between settling and resuspension due to shear diffusion. Other mechanisms have been proposed to explain the granular-front formation. On an incline, a free-surface flow produces a velocity profile that monotonically grows with the height. At the same time, if the grains are coarse, their concentration will be lower close to the base, because their centers cannot approach the wall at a distance smaller than their radius, and higher close to the free surface. Under this conditions, the average velocity of the particle on top will tend to be higher than that of the surrounding fluid [28]. For the case in which the flow is not laterally confined, the segregation process is active also in the transversal direction, which leads to the creation of more complex structures, such as lateral levees [7] or fingers [29]. Experiments on an incline are naturally limited to the study of a transitory state, due to the finite length of the geometry. Within the rotating drum, a stationary flow can easily be obtained, and its properties can be continuously measured. Moreover, the recirculation velocity of the material can be controlled directly by tuning the drum rotational speed, which allows one to focus on the settling behavior of the particles.

This is observed in detail by reproducing the experimental settings in a numerical environment. The used method is based on the well-established coupling between the discrete element method (DEM) for the representation of the particle phase, and the lattice-Boltzmann method (LBM) for the solution of the fluid phase [Figs. 1(c) and 1(d)]. The use of the DEM allows the tracking of every single particle, and the combined analysis of the behavior observed in the experiments and simulations provides the necessary parametric framework for the formulation of a nondimensional group, which predicts the granular-front formation. The results are not restricted to the field of natural hazards, since they potentially apply to the whole group of concentrated suspension [30,31], comprising materials such as fresh concrete and many pastes processed in the pharmaceutical and food industry.

This paper offers a description of the experimental (Sec. II) and numerical (Sec. III) setting, followed by the presentation of the results in Sec. IV and their interpretation in Sec. V. Section VI summarizes and comments on the conclusions.

## II. EXPERIMENTAL METHODS

The rotating drum employed throughout this study is located at the University of Natural Resources and Life Sciences (BOKU), Vienna, Austria, and described in detail in Refs. [32,34,35]. Therefore, only a brief description of the instrumentation and the configuration of the drum for the experiments in this study is presented. The rotating drum has a cylindrical shape with radius of $R = 1.23$ m and width $W = 0.45$ m (see Fig. 3). The cylindrical reference system used in this paper is presented in Fig. 3, with the angular

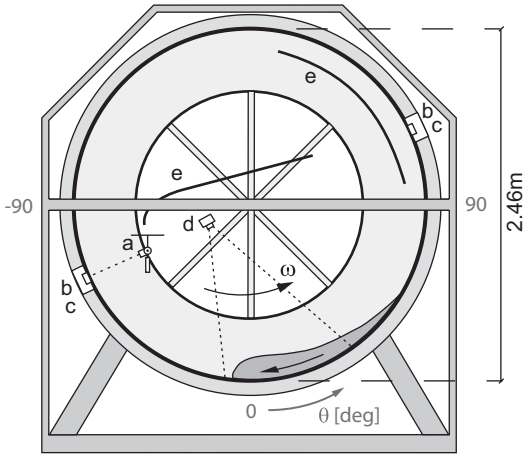


FIG. 3. Rotating drum at BOKU. (a) Height point laser, (b) normal load cell, (c) fluid pressure transducer, (d) high-speed camera, and (e) inner roofs (drop protection). Adapted from Refs. [32,33].

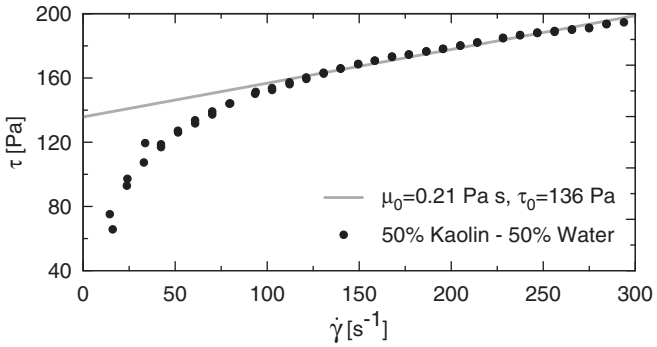


FIG. 4. Rheological behavior of the kaolin-water dispersion. The flow curve is approximated as a Bingham fluid (solid line).

coordinate $\theta$ being 0° at the 6 o'clock position and 90° and −90° at the 3 and 9 o'clock position, respectively. The sidewalls are composed at one side of stainless steel and at the opposite side of acrylic glass, while the bed of the channel is roughened using a rubber surface with protrusions in a zigzag pattern of approximately 3 mm in height and 5 mm in separation. Material losses are observed due to the clogging of material in the roughened bed, which then drops and accumulates at the inner roofs [Fig. 3(e)]. The loss of material is recognized as one of the major limitations of the tests conducted, and is noticeable for high viscous flows. In experiments, the drum rotates around its axis at a constant rotational speed $\omega$ of approximately 0.3, 0.5, 0.7, or 0.9 rad/s.

The material is chosen to represent a simplified natural suspension, resembling to some extent the one in a debris flow. Particles are ceramic balls of density $\rho_s = 2420$ kg/m$^3$ and diameter $d = 32.6 \pm 0.03$ mm, whose high strength and stiffness enables the occurrence of strong collisional forces without large deformations or material failure. The friction angle between the ceramic balls and the drum roughened bed material is $\psi_{bed} = 42.5°$, measured in a similar way as presented in Ref. [36], while the interparticle friction angle is $\psi_s = 27.7°$ [37]. Particles collide with a constant coefficient of restitution of $c = 0.7$ when dry, and $c \simeq 0$ when covered with fluid.

The fluid phase is obtained by mixing kaolin powder [particle size of 2.0 $\mu$m ($D_{50}$), and particle density of 2600 kg/m$^3$] with water. Changing the relative proportions of kaolin and water, mixtures of different rheological behaviors are obtained [28]. The parameters of the kaolin-water dispersion are measured using a simple co-axial cylinder rheometer (Bohlin Visco 88) with a gap of 1.5 mm. The mixture used in experiments is composed of kaolin and water in equal parts by mass, resulting in a fluid with density $\rho_f = 1420$ kg/m$^3$ and a rheological flow curve as presented in Fig. 4. For simplicity in the numerical analysis (Secs. III, IV), the resulting dispersion is assumed to behave like a plastic fluid with a yield stress $\tau_0$, whose constitutive relation between shear stress $\tau$ and shear rate $\dot{\gamma}$ is approximated with a Bingham law

$$\tau = \tau_0 + \mu_0 \dot{\gamma}, \tag{2}$$

where $\mu_0$ is the plastic viscosity (see Fig. 4).

The material inside the drum forms a stationary free-surface flow, whose front, body, and tail present distinct features. Along the channel axis, the front presents velocities both in the $\theta$ and $r$ directions, while in the body, velocities in $r$ are negligible [24]. At the tail the flow gives rise to unsteady avalanche releases [38].

In experiments, the drum is partially filled with a volume (net of losses) of 40 kg of fluid, together with a variable amount of particles (10, 20, 30, 40, 50 kg). This results in mixtures with a global particle concentration in the range of $\Phi = 13$, 23, 31, 38, and 43%, respectively.

The drum is instrumented as shown in Fig. 3. At every successive rotation, basal total load and basal fluid pressure are measured with a set of two load cells (HBM PW2GC3) and one piezoresistive pressure transmitter (Keller PR25Y), fixed normal to the bed and displaced 180° along the circumference. The load cells are connected to a plate, 60 mm in diameter, covered by the same roughened layer of the drum's bed. At the same time, the flow height is recorded by a point-laser sensor (Baumer OADM 20), rotating with the drum recording a height profile every turn of the drum. The revolution of the drum is continuously traced by a photoelectric sensor that records an impulse every degree of rotation. All instruments record at a sampling frequency of 1200 Hz. At this sampling frequency, a flow of 1.28 m long at drum velocities of 0.3 and 0.9 rad/s provides during each rotation a total amount of 1290 and 430 data points along the flowing mixture, respectively. In addition, a high-speed camera (Optronis CR3000x2) with a 28–200 mm lens records the front of the flowing material. The camera is mounted near the center of rotation of the drum, with a focal distance of 1.2 m to the channel bed. The videos are recorded at a frame rate of 500 fps, with a frame size of 1696 × 1710 pixels.

Height, basal load, and basal fluid pressure measurements are obtained from successive rotations, at a constant drum velocity, and condensed calculating the median of the measurements at every $\theta$ point. The resulting longitudinal profiles (see Fig. 8) enable identifying from the height profile the flow front position $\theta_{flow}$, flow height $h$, and flow length $l$, and from the fluid pressure profile the fluid front position $\theta_f$. By doing

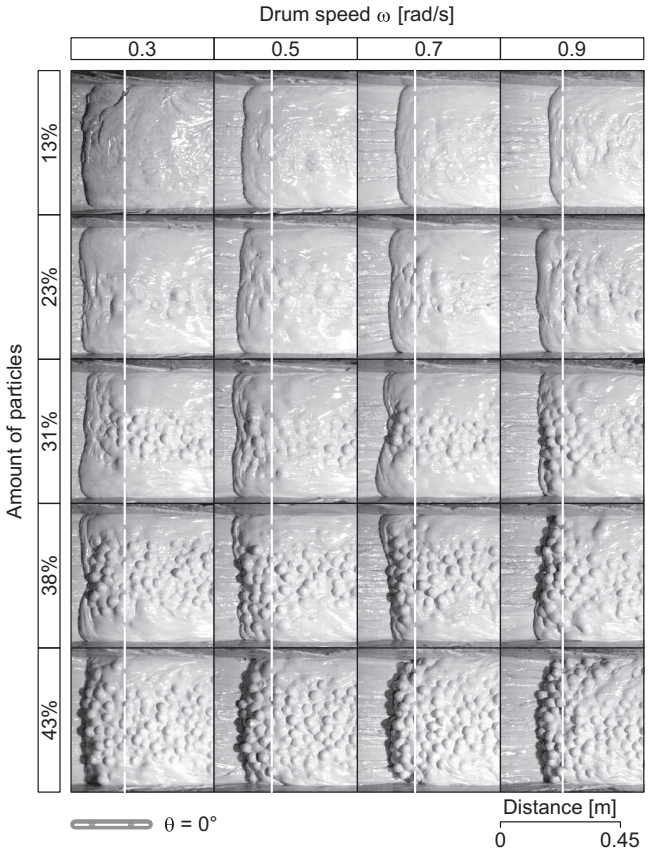


FIG. 5. Front as a function of the angular velocity of the drum and particle concentration.

so, it is possible to discern the location of the fluid front $\theta_f$ inside the flowing mixture's front $\theta_{flow}$.

As mentioned in the introduction, a transitory state can be observed, during which the oscillations of the front positions are larger. However, after less than 3 complete revolutions of the drum, which corresponds to a few seconds, the system reaches a steady state. The oscillations stabilize around equilibrium positions and the recording instruments are activated. This assumption is later on validated by the observation that all recordings of the flow height collapse on a single profile. During the stationary, the measurements are performed at constant omega over a series of at least 10 rotations. In experiments, no formation of fingers is observed.

A clear distinction between the fluid front and particle front is not possible to discern from the longitudinal height profiles. For this reason, the relative separation between fluid and particle front ($\Delta\theta = \theta_p - \theta_f$) is assessed from the sequence of frames obtained with the high-speed camera (see Fig. 5). In this analysis, each frame is binarized to enhance the front identification [Fig. 6(b)]. Over the resultant binary image, the front of the flowing material is detected with a Canny edge detector [39] as shown in Fig. 6(c). Fluctuations in time of the front detection are observed. Despite a nonclear periodicity, its variation is useful in the definition of the flow front variation in time as presented in the error bars of the flow front markers in Fig. 9. The accuracy of the flow front detection is inversely proportional to the intensity and width of the shadow at the

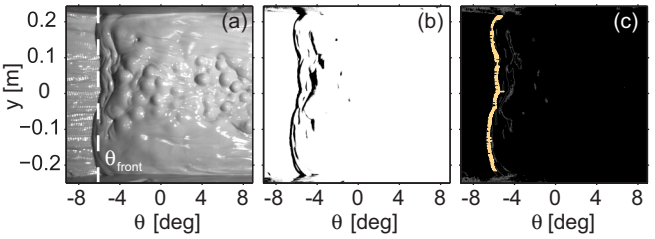


FIG. 6. (Color online) Image front detection analysis. (a) Raw image, (b) binary image conversion, and (c) Canny edge detector. The yellow line presents the location of the flow front and the vertical dashed line is the median flow front $\theta_{front}$.

front, ranging between 1.0° and 3.6°. The relative position of the particle front is manually inferred from the occurrence of particle bumps in the flow surface over a sequence of frames, with a related error of 1.8°.

Arranging experiments where the phenomenon is more pronounced would be relatively easy. Consistently with the interpretation we provided in Sec. V, this can be done by using more fluid, or a lower viscosity. However, tracking the particles becomes more difficult because the fluid is not transparent. The larger the fluid-particle front gap, the harder it is to identify the particle front with sufficient precision. For this reason we chose a mixture with an initial position for the particle front that is already close to the fluid front even at lower speed.

## III. OUTLINE OF THE LBM-DEM METHOD

The experimental setting described in the precedent chapter is recreated in a numerical environment. The natural choice for the simulation of the particle-fluid mixture is a hybrid DEM-LBM method, due to its flexibility to handle the many challenges posed by the nonlinear boundary conditions. The simulations allow one to track position and velocity of every single particle, to identify mechanisms and relevant phenomena occurring close the front. Furthermore, once the method is validated against the experimental results, the simulations are used to obtain more points, and to construct the continuous transition of the fronts with varying $\omega$, from 0.1 to 1.0 rad/s with steps of 0.25 rad/s. This work is also meant to be a further validation of the DEM-LBM method, which has been so far applied only to a limited number of real problems [40–42].

A detailed presentation of the numerical scheme is beyond the scope of the present work. The readers are referred to the literature on the LBM in Refs. [43,44] and on the DEM in Ref. [45]. The coupling between these two solvers has been the object of much recent research [46] and has nowadays achieved a high level of maturity, with the possibility to simulate real systems also with non-Newtonian fluids [47].

The domain is discretized in a fixed, regular, cubic lattice, whose nodes belong to these five categories: fluid, gas, interface, solid walls, or solid particle. The role and governing equations for every node type are described below.

*Fluid nodes* are the locations where the fluid dynamics is solved. This is realized through a discretization of the Boltzmann equation. The fluid is not represented by continuous fields of macroscopic variables, like in most classic

solvers, but rather through streams of microscopic particles, or populations, whose collisions and subsequent redistribution governs the dynamics. The population density $f$ at every fluid node is used to reconstruct density $\rho_f$, pressure $p_f$, and velocity $\boldsymbol{u}_f$ through simple summations. If $f_i$ describes a population moving at speed $\boldsymbol{c}_i$, this translates into

$$\rho_f = \sum_i f_i, \quad p_f = c_s^2 \rho_f, \quad \boldsymbol{u}_f = \sum_i f_i \boldsymbol{c}_i / \rho_f, \tag{3}$$

which implies that the fluid is actually treated like a slightly compressible medium, and the pressure is a secondary variable obtained by multiplication of $\rho_f$ with the square of the system speed of sound $c_s^2$. The evolution of $f_i$ during a unitary time step is governed by the lattice-Boltzmann equation

$$f_i(\boldsymbol{x} + \boldsymbol{c}_i, t+1) = f_i(\boldsymbol{x}, t) + \Omega_i(\boldsymbol{x}, t) + F_i(\boldsymbol{x}, t, \boldsymbol{g} + \boldsymbol{p}), \tag{4}$$

where $F_i$ implements the effect of gravity $\boldsymbol{g}$ and of the fluid-particle coupling term $\boldsymbol{p}$, while $\Omega_i$ is an operator describing the effect of population collisions. Commonly expressed by the Bhatnagar-Gross-Krook linear approximation [48], it relaxes the system to an equilibrium state $f_i^{\mathrm{eq}}$,

$$\Omega_i = \frac{f_i^{\mathrm{eq}} - f_i}{\tau}. \tag{5}$$

The transition to equilibrium is described by the relaxation time $\tau$, which is proportional to the plastic viscosity of the fluid $\mu_0$ and its yield stress $\tau_0$ [47] as

$$\tau = \frac{1}{2} + \frac{\tau_0/\dot{\gamma} + \mu_0}{c_s^2}. \tag{6}$$

*Gas nodes* represent the space not occupied by the fluid, and therefore neither contain nor transfer populations.

*Interface nodes* represent the interface between fluid and gas, and are similar to fluid nodes, in the sense that the streaming of population happens in an identical fashion. However, they are granted an additional degree of freedom, a variable called mass $m \in (0,1)$, used to track the evolution of the surface. Interface nodes mutate into fluid nodes if $m \geqslant 1$ or into gas nodes if $m \leqslant 0$. The evolution of mass depends on the difference between the populations streaming in and out of the node,

$$m(t+1) = m(t) + \sum \alpha (f_{\mathrm{in}} - f_{\mathrm{out}}), \tag{7}$$

where $\alpha$ depends on whether the population exchange happened between two interface nodes or between a fluid and an interface node [49]. The modeling of surface tension can be included in this formulation. However for the studied cases a set of test simulations revealed surface tension to have no sensible effect on the results, and its modeling has therefore been neglected.

*Solid wall nodes* are all nodes that lie inside solid walls, i.e., the drum cylinder and lateral walls. They do not contain nor transfer populations, but nevertheless affect the fluid since they both enforce no-slip at the boundary and transfer momentum to the fluid when the drum is in motion. No-slip is enforced by requiring all population streams $f_i$ pointing towards a solid node to be reflected back. The reflected populations $f_{i'}$ are modified taking into account the momentum transfer,

$$f_{i'} = f_i - 6 w_i \rho_f \boldsymbol{u}_w \cdot \boldsymbol{c}_i, \tag{8}$$

where $\boldsymbol{u}_w$ is the velocity of the wall at the reflection location and $w_i$ is a weight depending on the lattice configuration. Nodes belonging to the drum surface employ a modified version of this rule, to take into account the curvature of the boundary. Details about the curved-surface treatment can be found in Refs. [50,51].

*Solid particle nodes* are all nodes contained inside solid particles. For the particle-fluid coupling algorithm the direct forcing approach [52] is employed in a simplified form similar to the one described in Ref. [53]. A sketch of the interaction mechanism is given in Figs. 1(c) and 1(d). Particles are immersed in the fluid and are advected through the LBM regular grid. The difference between particle and fluid velocity is used to compute a hydrodynamic interaction force that is transmitted both to the fluid and to the particle equations of motion. The lattice-Boltzmann equation is solved in this case with the additional forcing term $\boldsymbol{p}$ appearing in Eq. (4), calculated as

$$\boldsymbol{p}(\boldsymbol{x}, t) = \rho_f(\boldsymbol{x}, t)[\boldsymbol{u}_f(\boldsymbol{x}, t) - \boldsymbol{u}_p(\boldsymbol{x}, t)], \tag{9}$$

where $\boldsymbol{u}_p$ is the velocity of the particle at the node location [54]. A force of opposite sign is applied to the particle.

Particle dynamics is solved using a DEM model [see Fig. 1(d)]. The collisions between particles, and the consequent momentum exchange, are modeled using a modified Hertzian law with constant coefficient of restitution (as in Ref. [55]). Whenever possible, we choose the simulation parameters in order to be equal to the measured properties of the experimental material. For the particles, some uncertainty is present on the determination of the shear damping coefficient, which was validated by qualitatively comparing the output of the simulations to the drum experiments (only particles). The restitution coefficient was estimated for particles covered by a thin film of fluid, which greatly reduces the elasticity of contacts. The material parameters used for the DEM are recapped in Table I.

The parameters for the fluid are taken directly from its measured properties; see Fig. 4. The representation of the rheological behavior with a linear law is only a rough approximation, whose effects are discussed in the next section. As highlighted in Sec. II, the total volume of the fluid mass is influenced by multiple losses, mainly located at the roof of the drum. The effective flowing volume is therefore back-calculated by fitting the shape of the flow in the simulations (without particles) to the one recorded by the point-laser

TABLE I. Material parameters used in the DEM.

| Parameter | Value |
|---|---|
| Mass density | 2420 kg/m$^3$ |
| Young's modulus | $1.6 \times 10^7$ Pa |
| Poisson's ratio | 0.3 |
| Restitution coefficient | $\simeq$0 |
| Shear damping | 10 kg/s |
| Particle-particle friction angle | 27.7° |
| Particle-drum friction angle | 42.5° |

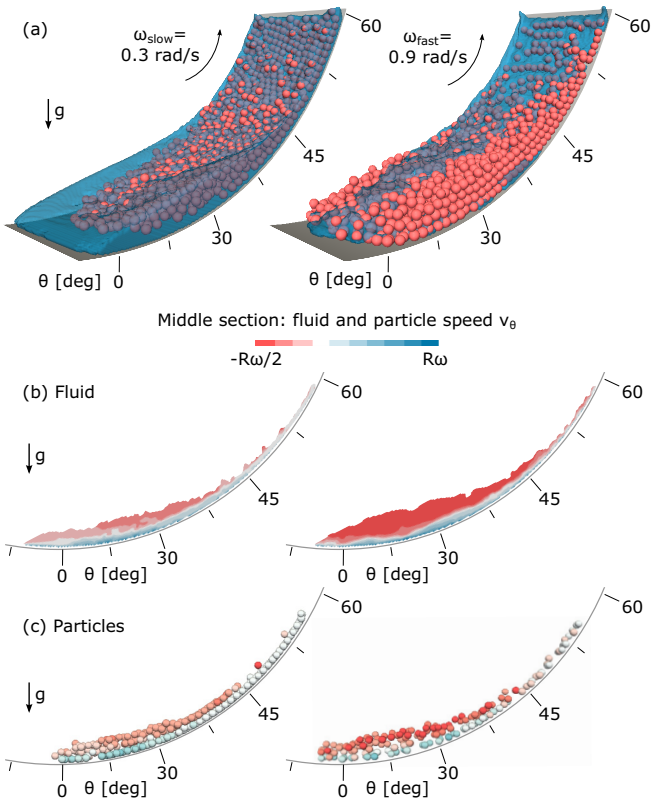


FIG. 7. (Color online) Snapshots of the DEM-LBM simulations (particle content of 31%). (a) The formation of a granular front by an increase in the angular velocity of the drum. The tangential velocity $v_\theta$ along a longitudinal profile for fluid (b) and particles (c).

sensor. Pictures from the simulations are shown in Fig. 7. The flow closely resembles the one observed in the experiments, and the same trend for the movement of the front is obtained.

## IV. COMPARISON BETWEEN NUMERICAL AND EXPERIMENTAL RESULTS

The height and the basal pressure longitudinal profiles obtained in the experiments described in Sec. II are used to validate the DEM-LBM scheme. Figure 8(a) presents the height profile as detected by the point-laser sensor and its numerical counterpart. Good agreement is found between the numerical simulation and the experimental measurements, matching reference points as the front location and flow height. In a similar way, the experimental basal pressure profile [Fig. 8(b)] coincides with the numerical pressure, accounting simultaneously for the particle and fluid contributions.

The most noticeable characteristic of the flow is the possibility to obtain a granular front even with a relatively low initial concentration of particles. The higher the rotational speed of the drum, the more particles will get close to the fluid front. The formation of a granular front strikingly resemble the one observed in a debris flow. This process is shown in Fig. 9, where the evolution of $\theta_f$ and $\theta_p$ found on experiments (markers) is compared with the numerical simulations (continuous lines). The distribution of the particles over the whole flow is computed from the simulation data, and shown with

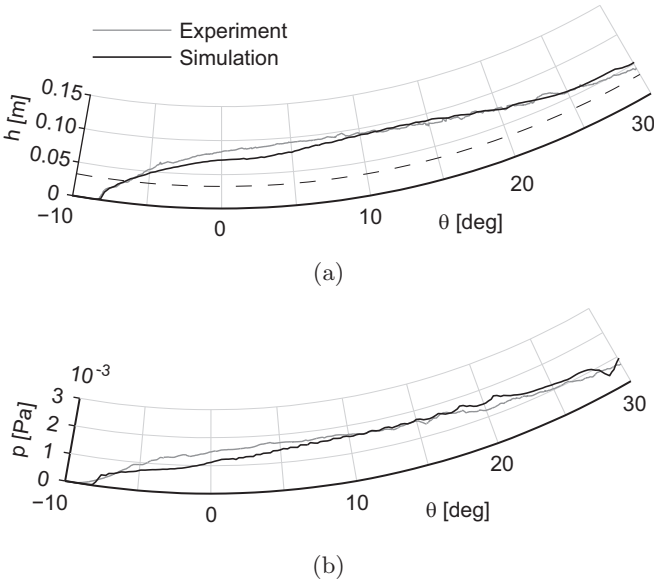


FIG. 8. Experimental and numerical flow height (a) and bulk basal pressure profiles (b) at 0.3 rad/s and particle concentration of 31%. The dashed line has the height of one particle diameter.

a gray-scale contour map. Good agreement is found on the flow front identification, which shows an asymptotic behavior towards higher drum velocities $\omega$. Experiments and numerical simulations fairly agree on the relative separation between the two phases $\Delta\theta = \theta_p - \theta_f$, which is a good indicative in the identification of the granular front. The center of volume of the flow $\theta_c$ is also shown in the figure. Experiments and numerical simulations show slightly different values for $\theta_c$, but follow similar trends.

The largest difference between experiments and simulations is observed at low drum velocities $\omega$, where the simulations predict a higher particle front than in the experiments, i.e., $\theta_{p,num} > \theta_{p,exp}$. The difference can be imputed to two effects. The first is due to the discretization of the fluid, which is unable to resolve the thin liquid film between the particles and the drum surface, when these two are in contact. This introduces an additional cohesive force between particle and drum, which is in general negligible, since this artificial cohesion is easily disrupted by the collision between particles. This is not so if the drum rotates very slowly, since the particles rearrange in a crystalline packing that is not easily broken. The second is due to the use of a Bingham law for the fluid, which best approximates the actual rheological curve only at high shear rates. If the drum rotates slowly, the maximum shear rates in the fluid stays below 50 $s^{-1}$, which results in a larger viscosity in the model compared to reality (see Fig. 4).

In agreement with Ref. [22], the transition from a fluid front into a granular front can be induced by an increase in the angular velocity of the drum (see Fig. 5). At low angular velocities, the particles are concentrated at higher inclinations. Then, with increasing velocities at the base, the particles diffuse, and start to move towards lower inclinations. Along with the motion of the particles, the interstitial fluid is strongly sheared by the particle motion and the drum bed. As a result of

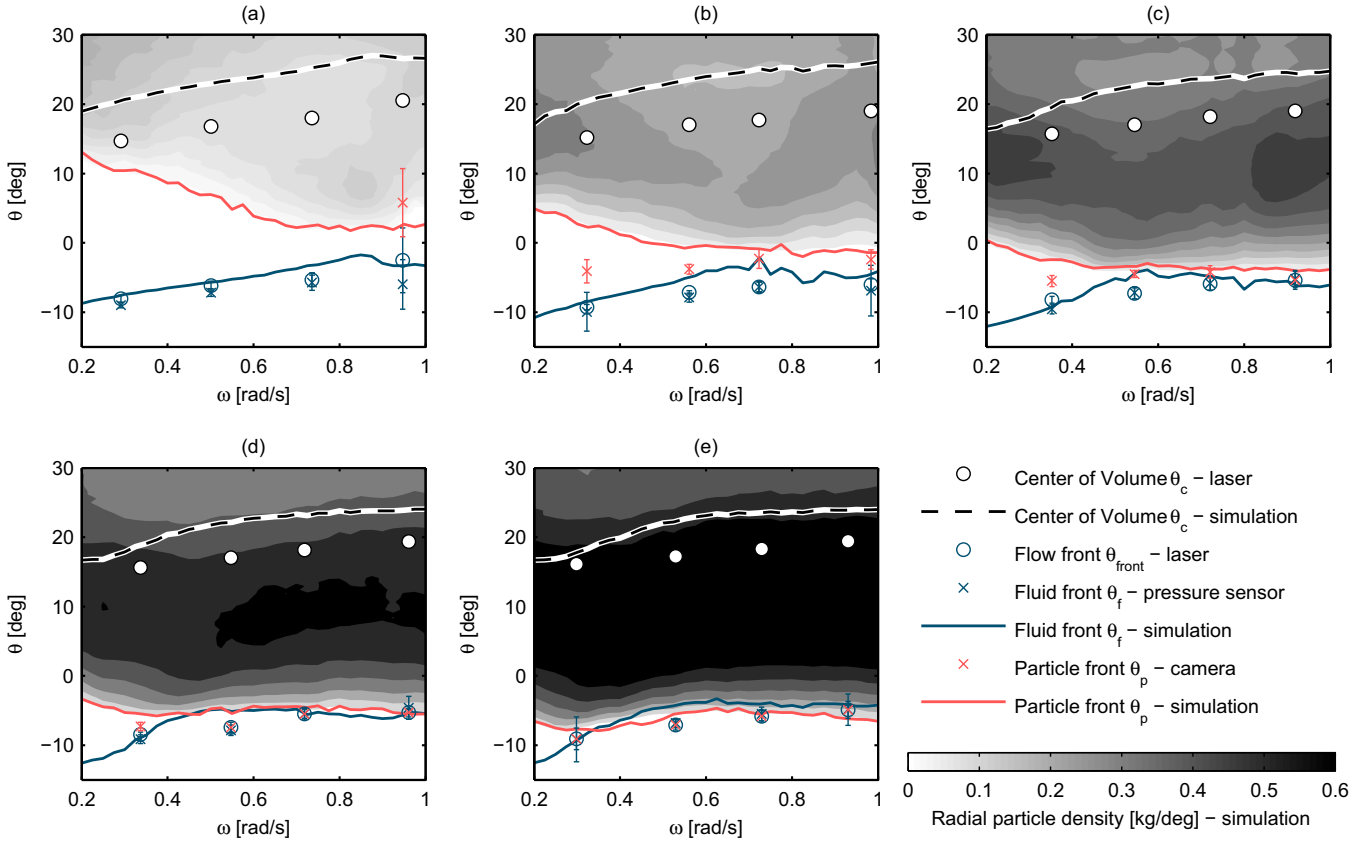


FIG. 9. (Color online) Experimental and numerical values for the position of fluid front $\theta_f$ (blue), particle front $\theta_p$ (red), and center of volume $\theta_c$ (white) vs drum speed $\omega$ for (a) 13%, (b) 23%, (c) 31%, (d) 38%, and (e) 43% particle content. Markers are obtained from experimental measurements at 4 different drum speeds $\omega$ (see Sec. II), while numerical simulations are performed every 0.25 rad/s (see Sec. III). The gray-scale contour map describes the particle accumulation in the mixture as obtained from the simulations.

this shearing, the fluid front moves upwards while the particle front move downward until the granular front is formed.

## V. INTERNAL MECHANISMS GOVERNING PHASE SEPARATION

The emergence of granular fronts, described in the previous section, is the result of two mechanisms. The first is the upward (i.e., in the positive $\theta$ direction) migration of the center of the flowing mass $\theta_c$. This movement, for fluid and particles alike, is observed for growing angular velocity of the drum; see Fig. 9. The fluid front $\theta_f$ follows the same trend, and shifts upwards as well. The particle front $\theta_p$, on the other hand, keeps a stable position or moves slightly upstream, in the opposite direction. This second mechanisms is independent from the overall behavior of the flow, and is explained by analyzing the dynamics of the particles at the front. Simple analytical models for these two phenomena are described in the following.

### A. The position of the fluid front

As seen in Fig. 4, the Kaolin-water mixture can be approximated with a Bingham fluid, characterized by a yield stress $\tau_0$ and a plastic viscosity $\mu_0$. On the one hand, the approximation is rough at low shear rates, and becomes quite good only for $\dot{\gamma} > 100$, which is reached only by the experiments performed at the highest drum speeds. Nevertheless, the Bingham law allows the reconstruction of an analytical solution, which might not quantitatively predict the features of the flow, but helps nevertheless to understand the observed behavior of the fluid. Obtaining this analytical solution using the Navier-Stokes equations for a Bingham plastic in the partially filled rotating drum is however not an easy task: The fluid presents a free surface whose shape is not given a priori. However, considering a single slice of the drum ($\theta$ fixed) and approximating it with a two-dimensional flow in the ($\theta$,$r$) plane, an approximate solution can be obtained, which is analogous to the use of a long-wave approximation [56]. This is valid only in the body of the flow, where the component $v_r$ is small compared to $v_\theta$ [24]. With this hypothesis the flow is assumed to be steady and self-similar over the width $W$ of the drum and the edge effects due to the side walls of the drum are neglected. The shear rate and shear stress tensors each boil down to one component $\dot{\gamma}_{\theta r} = \frac{\partial v_\theta}{\partial r}$ and $\tau_{\theta r}$. The Bingham constitutive law can be written in this new system as

$$\begin{cases} \left|\frac{\partial v_\theta}{\partial r}\right| = 0 & \text{if } (|\tau_{\theta r}| < \tau_0), \\ \tau_{\theta r} = \left(\frac{\tau_0}{\left|\frac{\partial v_\theta}{\partial r}\right|} + \mu_0\right)\frac{\partial v_\theta}{\partial r} & \text{if } (|\tau_{\theta r}| > \tau_0). \end{cases} \quad (10)$$

The integration of the momentum equation with limits $r = R$ at the base of the drum, and $r = r_h$ at the free surface position,

gives the solution of the tangential-velocity profile $v_\theta(r)$:

$$\begin{aligned} &\omega R - a\sin\theta(r-R)(r+R-2r_0) && \text{if } r_0 < r < R,\\ &\omega R - a\sin\theta(R-r_0)^2 && \text{if } r_h < r < r_0, \end{aligned} \quad (11)$$

where $\omega$ is the rotational speed of the drum, and $a = \rho_f g/2\mu_0$. Between the positions $r_0$ and $r_h$ a plug flow forms, whose total height $h_0 = r_0 - r_h$ is proportional to the yield stress as

$$h_0 = \frac{\tau_0}{\rho_f g \sin\theta}. \quad (12)$$

By imposing stationary conditions, and therefore total flux $q_\theta = 0$ in the $\theta$ direction, the total height of the fluid $h = R - r_h$ is obtained. The following expression can be obtained by integrating the velocity profile [Eq. (11)] over the whole height $h$ (both yielded and unyielded regions):

$$q_\theta = \omega R h - \tfrac{1}{3} a \sin\theta (h-h_0)^2(2h+h_0) = 0. \quad (13)$$

This equation can be solved numerically to obtain the height $h$ of the flow. An elegant solution can be extracted with the approximation $2h + h_0 \approx 3h$, which is justified by $h_0$ being of the same order of $h$. Thus

$$h \approx h_0 + \sqrt{\frac{\omega R}{a\sin\theta}}. \quad (14)$$

Dividing this expression for the initial level $h_0$ provides a mean to predict the the increase in total height of the flow $h$ as a function of the drum speed $\omega$. This reads

$$h^* = \frac{h}{h_0} \approx 1 + \sqrt{\frac{2\mu_0\rho_f g\omega R\sin\theta}{\tau_0^2}}. \quad (15)$$

This solution does not hold for positions in the flow where a nonnegligible $r$ component exists, like the flow front. In addition, it is a general solution that does not take into account the actual flowing volume. For these reasons, it cannot be used to reconstruct the height profile over the whole range of $\theta$. However, for positions in the drum sufficiently far from the front ($\theta > 10^\circ$), Eq. (15) qualitatively captures the trend of variation of the height as linear function of the square root of the drum rotational speed $\sqrt{\omega}$. This is so because at higher basal velocities, in order to keep a stationary motion, the fluid needs to accumulate mass by increasing its height, an effect typical for free-surface flows of shear-dependent fluids. Figure 10 shows the fluid height measured in experiments and simulations as a function of $\sqrt{\omega/\omega_{\max}}$ (with $\omega_{\max} = 1.0$ rad/s). The average height $\bar{h}$, calculated averaging the flow height $h$ in the range of $25^\circ \leqslant \theta \leqslant 30^\circ$, is plotted, showing a good agreement with the linear trend predicted by Eq. (14).

Since the flowing volume is constant, the rise of the fluid height given by Eq. (14) must be accompanied by a transfer of mass from the front. This explains why the fluid front moves upwards when the angular velocity of the drum is growing (see Fig. 9). The increase in the front position $\theta_f$, follows the same proportionality to the square root of the angular velocity of the drum $\sqrt{\omega}$, see Fig. 11, as long as the influence of particles is minimal. The position of the center of volume of the flow $\theta_c$ follows a similar trend (see Fig. 9). In a fluid-only scenario (black solid markers), the relationship $\theta_f \propto \sqrt{\omega}$ holds true for the whole range of simulated velocities. For simulations with particles, there is an initial linear trend, followed by an abrupt variation. This corresponds to the point when the particles get closer to the fluid front, which then becomes dominated by particle dynamics. For the limit of a very high particle content

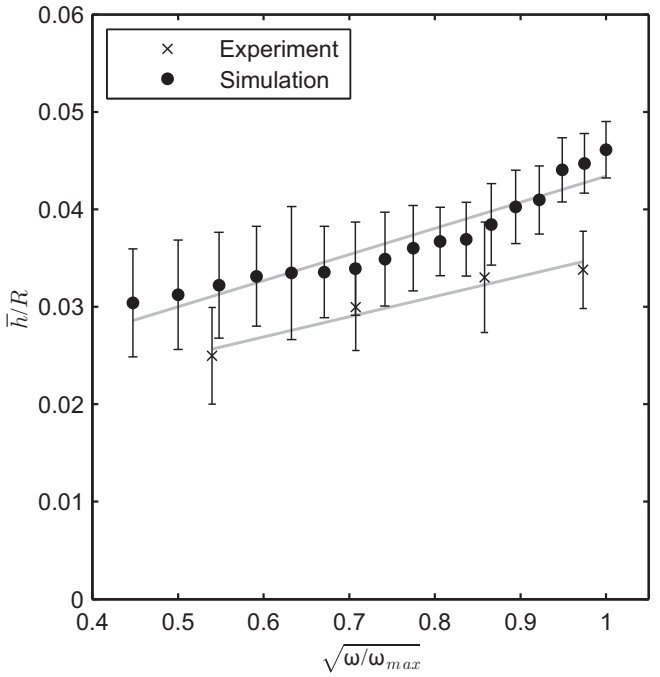


FIG. 10. Analytical flow height of a free surface flow down an incline against the experimental and numerical height (average height between 25° and 30°). The solid lines are fit to the data points and highlight the linear behavior.

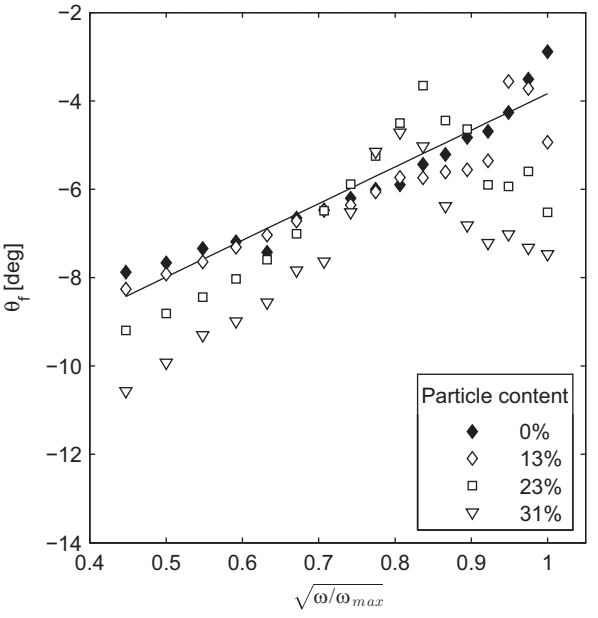


FIG. 11. Numerical location of the fluid front $\theta_f$ as a function of the angular velocity of the drum $\omega$. Markers represent different particle contents. For a fluid-only simulation the trend is linear (solid line).

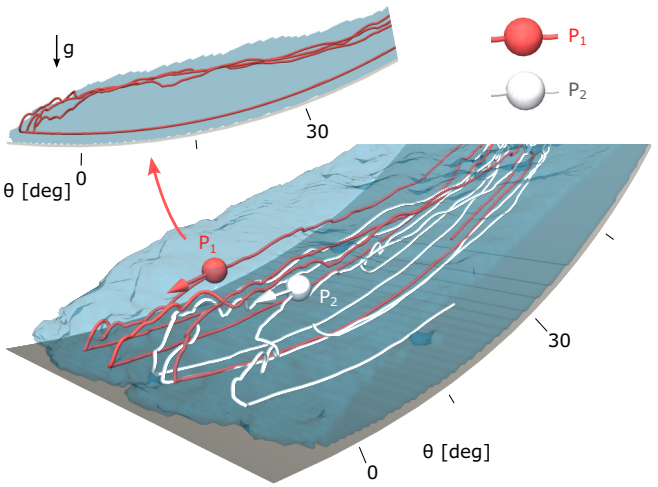


FIG. 12. (Color online) Qualitative representation of the particle trajectories. The position of two representative particles is tracked through the whole simulation, showing how the recirculation pattern continuously draws particles to the front, where they settle. Once the particles reach the bottom, they are drawn back towards the tail.

the linear trend is completely absent, and the behavior of the front can only be explained through the behavior of particles.

### B. Dynamics of the particles close to the front

In Fig. 9 the position of center of the flow $\theta_c$ shows a tendency to shift upwards when the drum rotates at higher velocities. As analyzed in the previous section, this happens because the flowing mass has to find a new equilibrium between downward and upward fluxes, which for higher speeds is only possible at higher inclinations. For the fluid, this results in a consistent variation of the position of the front, which also moves upwards. The particle front, on the other hand, follows a different trend. At growing angular velocities of the drum, $\theta_p$ either keeps a stationary position, or moves slightly downwards, i.e., in opposite direction to the fluid front. This counter-intuitive effect can be explained by looking at the behavior of particles located close to the front. Particles follow a similar recirculation pattern to the one of the fluid, with a downward flux close to the free surface and an upward flux close to the bottom. Additionally, the particles are settling in the direction of gravity. This induces a third flux, in the vertical direction, that completes the cycle. Figure 12 presents this recirculation pattern. Every single particle reaches the front multiple times, where it settles before being dragged upwards. This process is idealized in Fig. 1(e) using a downward travel flux, an upward travel flux, and a settling flux, characterized by their velocities $u_t^{down}$, $u_t^{up}$, and $u_s$, respectively. The travel fluxes happen in the circumferential direction $\theta$ while the settling flux is vertical. For a position close to the front ($\theta \simeq 0$), the circumferential and vertical fluxes are almost orthogonal, and can be analyzed separately. In the following, the settling velocity $u_s$ and the time scale of the settling process $t_s$ are supposed to be independent of the drum speed. The settling time scale $t_s$ determines how long it takes for a particle to settle from a top position, where it is subject to the downward flux, to a bottom position, where it is subject to the upward flux. If this process is slow, i.e., $t_s$ is large, the top particles will stay for a long time in the downward flux, therefore being dragged towards the front. The downward flux velocity $u_t^{down}$ determines a travel time scale $t_t$ which represents the time it takes for a particle to reach the front, following this flux. In this order of ideas, if $t_t$ is shorter than $t_s$, a granular front can potentially form.

Figure 12 also shows how particles tend to shift towards the sides while recirculating (in the figure, $P_1$ to the right and $P_2$ to the left), a phenomenon linked to levee formation in natural flows [4,7].

To get an estimate of $t_s$, the equation of motion for an immersed spherical particle subjected to gravity and buoyancy is solved:

$$\frac{\pi}{6}\rho_p d^3 \frac{du_r}{dt} = \frac{\pi}{6}\Delta\rho g d^3 - \frac{\pi}{8}\rho_f d^2 C_D u_r, \tag{16}$$

with $C_D$ the drag coefficient, and $\Delta\rho = \rho_p - \rho_f$ the density difference. The solution of Eq. (16) returns a settling velocity $u_s$ under stationary condition of

$$u_s = \sqrt{\frac{4}{3}\frac{d\Delta\rho g}{\rho_f C_D}}. \tag{17}$$

The drag coefficient $C_D$ plays a key role, since it determines the speed at which a granular system will react to an external perturbation by reorganizing its structure [57–59]. In the present work, two different settling conditions are present, depending on whether the particles are immersed in the fluid or in air, i.e., whether a granular front has been formed or not. If the particle front is still immersed in the fluid ($\theta_p > \theta_f$), a condition that is common for low drum speeds, the particles will settle while completely surrounded by the fluid. Due to the high viscosity, in this state the drag coefficient $C_D^{fluid}$ is high, and as a consequence the corresponding settling velocity $u_s^{fluid}$ is small. On the opposite, if the granular front is completely developed ($\theta_p \simeq \theta_f$, or $\theta_p < \theta_f$), some of the fluid in the space between the particle will be substituted by air. Particles will then potentially reach a higher settling velocity $u_s^{air}$ due to the lower $C_D^{air}$.

The correct determination of $C_D^{fluid}$ is a challenging task. For the case of a single-particle settling in a Bingham plastic, there exist empirical solutions that link the drag coefficient to the Reynolds number and to the plastic properties of the fluid [60–63]. Such solutions are accurate for the case of a single particle, but need to be adjusted for the case of a many-particle settling, and rewritten as a function of the particle concentration $\phi$. This correction requires a description of the position of the yield surface around the particles, as well as the determination of the effect of collisions, and its analytical determination goes beyond the scope of this work. An estimation of it can be obtained using the data from the DEM-LBM simulations. Figure 13 shows the average particle velocity in its vertical component, calculated in the simulations in proximity to the front ($\theta_p \leqslant \theta \leqslant \theta_p + 2.5°$). As long as the particle front remains completely immersed (low $\omega$), the velocity $u_s$ is roughly equal to $u_s^{fluid}$, and keeps being constant, which is justified by its expression [Eq. (17)], being a function of material properties only, and therefore invariant with respect to the drum speed. Its value however changes as soon as

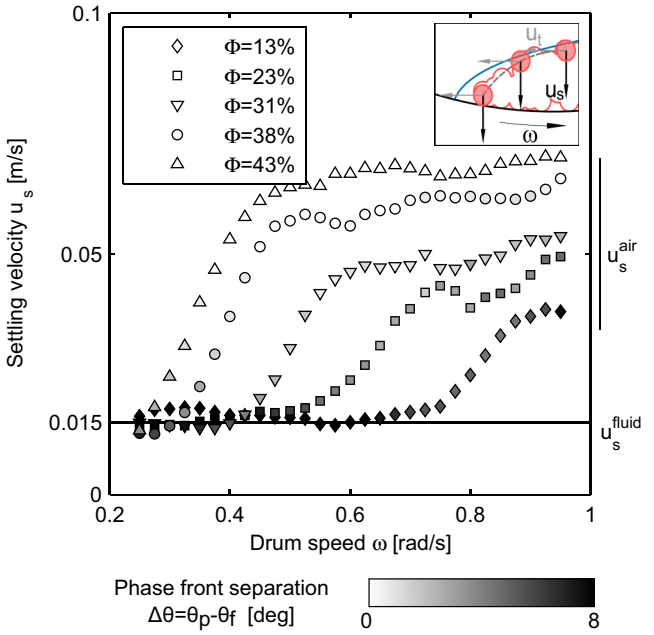


FIG. 13. (Color online) Settling velocity of the front particles, calculated using the simulations by averaging the vertical velocity of the particles in the range $\theta_p \leqslant \theta \leqslant \theta_p + 2.5^\circ$. The marker shape indicates the composition of the flow, while the shading shows whether the fronts are separate (dark shades) or merged (light shades). When the fronts are separate, the settling velocity is equal to the settling velocity in the fluid $u_s^{\text{fluid}}$. This increases as soon as the two fronts get closer, because some particles fall no more through the fluid, but rather through a mixture of air and fluid, therefore reaching a higher velocity $u_s^{\text{air}}$.

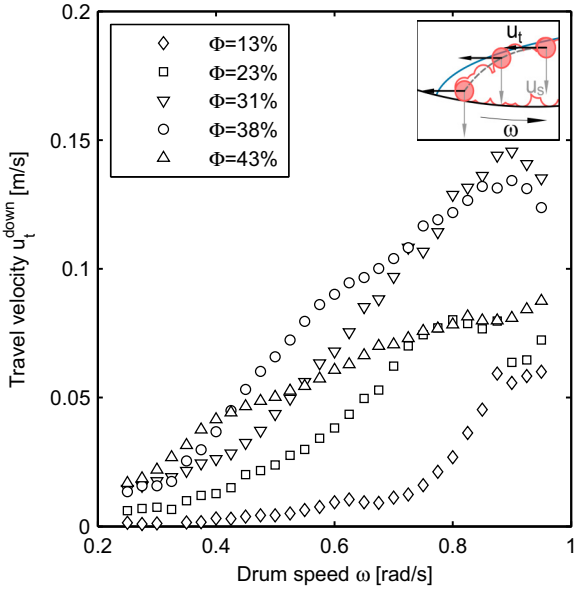


FIG. 14. (Color online) Travel velocity $u_t^{\text{down}}$, calculated using the simulations by averaging the horizontal velocity of the particles laying on the top layer in the range $\theta_p + 2.5^\circ \leqslant \theta \leqslant \theta_p + 5.0^\circ$. The markers represent the composition of the flow. For the case of 13% particles, there is no recirculating flow if $\omega < 0.6$ rad/s, and this velocity is close to zero. Elsewhere, a recirculating flow develops, and the velocity is correlated to the drum speed. The relative positions of the fronts does not seem to influence the travel velocity.

particle and fluid fronts get close, since the particles are no more completely immersed. A transition can be observed between $u_s^{\text{fluid}}$ and $u_s^{\text{air}}$, which correspond to the formation of the granular front. Once this is completely developed, the final settling velocity is again roughly invariant with $\omega$, and equal to $u_s^{\text{air}}$. This further justifies the hypothesis of the settling process to be independent of the downstream and upstream flux velocities, since there is no direct correlation between $u_s$ and $\omega$. Note that there is no single $u_s^{\text{air}}$, but mixtures with different particle content exhibit different values. This is due to the fact that the particles at the front do not fall for a time sufficiently long to reach their terminal velocity. The more particles are in the system, the thicker is the particle layer, and the velocity that the particles can reach falling through it. Note that once the granular front is completely formed, $u_s$ is again invariant with respect to $\omega$.

The particles which take longer to settle to the bottom of the flow are the ones laying on top of the granular mass, since they have to pass through its whole height $h_p$. Increasing the number of particles causes the flow to expand in height $h_p$ and length $l_p$, but not in width, since this is fixed by the drum width $W$. For this reason, the level $h_p$ can be assumed to be proportional to $\sqrt{V_p/W}$, with $V_p$ the total volume of particles. The maximum settling time can be therefore estimated as

$$t_s^{\text{fluid}} \simeq \frac{h_p}{u_s^{\text{fluid}}} \simeq \sqrt{\frac{3}{4}\frac{V_p}{W}\frac{\rho_f C_D^{\text{fluid}}}{d\Delta\rho g}}. \qquad (18)$$

The same particle has also a velocity in the $\theta$ direction, due to the recirculating pattern of the flow. If the particle is close to the free surface, this velocity is $u_t^{\text{down}}$ (downstream), while if it is close to the bottom of the granular mass, it is $u_t^{\text{up}}$ (upstream). This pattern can be observed also by looking at the velocity of the single particles, as visible in Fig. 7(b). The higher $u_t^{\text{down}}$ is, the further the top particles can travel downstream. This velocity can be determined using the data from the simulations, recording the velocity in the circumferential direction of the particles on the top layer of the flow, right behind the particle front ($\theta_p + 2.5^\circ \leqslant \theta \leqslant \theta_p + 5.0^\circ$). The time-averaged results are shown in Fig. 14. A rough linear proportionality $u_t^{\text{down}} \propto \omega R$ can be seen. This is because the recirculating velocity of the particles is enforced by the boundary condition at the wall, i.e., the velocity of the drum, and by the drag exerted by the recirculation of the fluid, which is also proportional to the drum speed. The velocity $u_t^{\text{down}}$ can therefore be considered to be directly correlated with $\omega$. The particles close to the free surface are traveling downstream and can potentially cover the distance between the particle bulk and the fluid front, $\Delta x$, if the settling process is sufficiently slow. The distance $\Delta x$ is related to the amount of free fluid, i.e., the fluid that is not trapped in the particle pores, $\Delta V = V_f - (1-\phi)V_p$, where $\phi$ is the particle volume fraction inside the particle layer, which can be assumed to be close to its maximum value, $\phi_{\max} = 0.55$. The initial gap $\Delta x$ can be directly related to $\Delta V$, and considering that the flow width $W$ is fixed $\Delta x \propto \sqrt{\Delta V/W}$. Moreover, as seen in the treatment for the fluid front, this distance is reduced at growing $\omega$ by the transfer of fluid mass between front and body of the flow. Using Eq. (15) to estimate this phenomenon,

the expression for the initial gap $\Delta x$ reads

$$\Delta x \propto \frac{1}{\overline{h}^*}\sqrt{\frac{\Delta V}{W}}, \tag{19}$$

where $\overline{h}^*$ is the average value of $h^*$ in the body of the flow (10° to 30°). The travel time can therefore estimated to be

$$t_t = \frac{\Delta x}{u_t^{\text{down}}} \simeq \frac{1}{\omega R \overline{h}^*}\sqrt{\frac{\Delta V}{W}}. \tag{20}$$

### C. The development of a granular front

The time scales defined in the previous section are useful to understand the transition from separated phases to a granular front. The ratio between the estimated time scale of travel and the time scale of settling through the fluid gives the following dimensionless quantity:

$$\xi = \frac{t_t}{t_s^{\text{fluid}}} = \frac{u_s^{\text{fluid}}}{\omega R \overline{h}^*}\sqrt{\frac{\Delta V}{V_p}}. \tag{21}$$

In this definition, $\xi$ is calculated using the value of $u_s^{\text{fluid}}$ extracted from the simulations, and therefore it is presumed that the fronts are separated ($\Delta\theta > 0$), or at least that the particles are immersed. If $t_s^{\text{fluid}}$ is larger than $t_t$, and therefore $\xi$ is small, the particles on the top layer will have time to reach the fluid front following the fluid streamlines, before they settle (a process governed by the settling velocity $u_s^{\text{fluid}}$). Figure 15 shows the angular distance between particle front and fluid front $\Delta\theta$ plotted as a function of $\xi$. On this plot, three different regimes can be observed. In the central part, the fronts are separated ($\Delta\theta > 0$), and the numerical data points aggregate around a line, which shows that the definition of $\xi$ well captures the trend leading to the development of a granular front. This

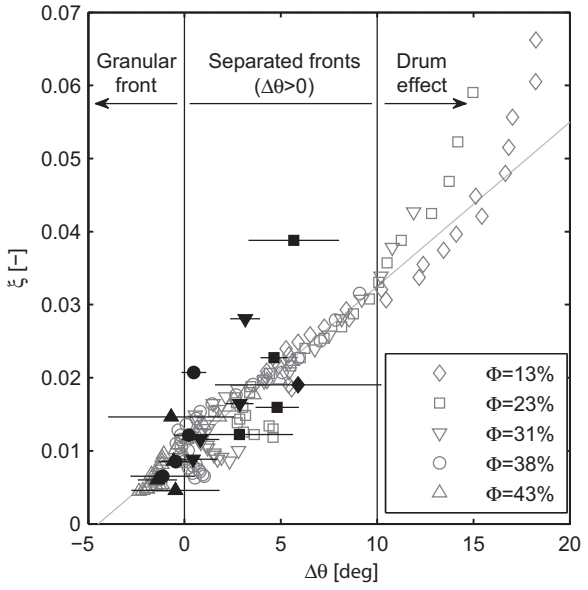


FIG. 15. Angle separating the particle front and the fluid front $\Delta\theta$ as a function of the time-scale ratio $\xi$. If the two fronts are separate, the data collapse on a lineal trend (continuous line). The simulation data are presented with gray markers, and experimental data with black markers.

stops holding true if the gap is too large, since the curvature of the drum starts to play an important role. Consider that, if $\omega \to 0$, no recirculation occurs, and the separation $\Delta\theta$ adjusts itself to the quasistatic equilibrium (a finite value), in contrast to the diverging behavior of $\xi$. The bottom-left part of the graph represent the fully developed granular front, where $\Delta\theta$ is small. For the geometry analyzed in this paper, the transition to this state corresponds to a threshold limit value of $\xi$ located between 0.01 and 0.02. Close to this threshold and below, most of the assumptions used in this section stop holding true, and the tendency is clearly no longer linear.

## VI. CONCLUSIONS

We presented a series of experiments to study the behavior of a mixture of fluid and particles inside a rotating drum. Particles are heavier than the fluid and therefore have the natural tendency to settle. This is contrasted by enforcing a recirculation of the material through the rotation of the drum. A sufficiently high angular velocity of the drum produces a front dominated by particles. This reorganization pattern of fluid and particle phases is typical for suspensions, both natural (e.g., debris flow) and industrial (e.g., fresh concrete). The same results are obtained in a numerical setting, using a hybrid method that combines LBM for the solution of the fluid phase with DEM for particle motion. Experiments and simulations show excellent agreement.

The phase-separation pattern is dependent on two phenomena. The first is the migration of the fluid front upwards, which can be observed for growing angular velocities of the drum. This is explained by looking at the analytical solution for the free-surface flow of a Bingham fluid down an incline. At the same time, the particle front either keeps a stationary position, or moves slightly downstream. The ratio between the time scale of settling and the time scale of particle recirculation defines a dimensionless quantity, $\xi$, that controls the formation of a granular front. The distance between particles and the fluid front is governed by $\xi$, which is proportional to the square root of the global particle content, and inversely proportional to the angular velocity of the drum. This result is confirmed by the simulation results. When plotting $\xi$ against the distance between particles and fluid front, numerical and experimental data roughly collapse on a line. The time-scale ratio $\xi$ depends on the asymptotic settling velocity, which is a quantity monotonically increasing with the particle size and monotonically decreasing with the viscosity of the fluid. The effect of the variation of these two parameters has been already observed in Ref. [22]. However, the exact influence of viscosity and particle size can only be tested with an extended experimental campaign using particles and fluids with variable properties, which we reserve for a later work. Note that if the yield stress becomes high enough to hinder the settling of particles, the framework proposed here needs to be integrated with further phenomena, such as shear-induced settling [61,62]. The validity of the $\xi$ scaling can be pivotal for the understanding of the free-surface flow of particle suspensions. In particular, it can lead to better understanding of the condition under which a debris flow can develop, or a fresh concrete mixture will segregate during casting.

**ACKNOWLEDGMENTS**

This paper is the result of a collaboration between the groups at ETH Zurich and BOKU Vienna, and between the first two authors. A.L. and M.C contributed equally to this work, and share first authorship. The research leading to these results has received funding from the People Programme (Marie Curie Actions) of the European Union's Seventh Framework Programme FP7 under the MUMOLADE ITN project (Multiscale Modelling of Landslides and Debris Flow) with REA Grant Agreement No. 289911, as well as from the European Research Council, Advanced Grant No. 319968-FlowCCS. The authors thank the *Kamig Österreichische Kaolin- und Montanindustrie* for providing the kaolin (Kamig E1) used in the experiments. Special thanks go to Dr. L. te Kamp and B. Wöhrl for ongoing support within the ITN.

[1] T. Takahashi, in *Debris Flow, Mechanics, Prediction, and Countermeasures* (Taylor & Francis, London, 2007), p. 464.
[2] O. Hungr, S. Evans, M. Bovis, and J. Hutchinson, Environm. Eng. Geosci. **7**, 221 (2001).
[3] J. M. N. T. Gray and C. Ancey, J. Fluid Mech. **629**, 387 (2009).
[4] C. G. Johnson, B. P. Kokelaar, R. M. Iverson, M. Logan, R. G. LaHusen, and J. M. N. T. Gray, J. Geophys. Res.: Earth Surf. **117**, F01032 (2012).
[5] B. Marks and I. Einav, Granular Matter **13**, 211 (2011).
[6] Y. Nohguchi and H. Ozawa, Physica D **238**, 20 (2009).
[7] A. Mangeney, F. Bouchut, N. Thomas, J. P. Vilotte, and M. O. Bristeau, J. Geophys. Res.: Earth Surf. **112**, F02017 (2007).
[8] J. Zhou, B. Dupuy, A. L. Bertozzi, and A. E. Hosoi, Phys. Rev. Lett. **94**, 117803 (2005).
[9] K. M. Hill, N. Jain, and J. M. Ottino, Phys. Rev. E **64**, 011302 (2001).
[10] F. Pignatel, C. Asselin, L. Krieger, I. C. Christov, J. M. Ottino, and R. M. Lueptow, Phys. Rev. E **86**, 011304 (2012).
[11] S. Chou and S. Hsiau, Powder Technol. **226**, 99 (2012).
[12] B. Turnbull, Phys. Rev. Lett. **107**, 258001 (2011).
[13] C. C. Liao, S. S. Hsiau, and H. C. Nien, Phys. Rev. E **89**, 062204 (2014).
[14] R. Yang, R. Zou, and A. Yu, Powder Technol. **130**, 138 (2003).
[15] N. Jain, J. M. Ottino, and R. M. Lueptow, Phys. Fluids **14**, 572 (2002).
[16] Y. Ding, R. Forster, J. Seville, and D. Parker, Chem. Eng. Sci. **56**, 3737 (2001).
[17] E. Clément, J. Rajchenbach, and J. Duran, Europhys. Lett. **30**, 7 (1995).
[18] G. Baumann, I. M. Jánosi, and D. E. Wolf, Phys. Rev. E **51**, 1879 (1995).
[19] G. H. Ristow, Europhys. Lett. **28**, 97 (1994).
[20] S. Brown, The vertically rotating flume for use as a rheometer, Ph.D. thesis, University of Missouri-Rolla, 1992.
[21] R. J. Huizinga, J. Hydraul. Eng. **122**, 456 (1996).
[22] R. Kaitna, L. Hsu, D. Rickenmann, and W. E. Dietrich, in *5th International Conference on Debris-Flow Hazards Mitigation: Mechanics, Prediction, and Assessment*, edited by R. Genevois, D. L. Hamilton, and A. Prestininzi (Casa Editrice Università La Sapienza, Rome, Italy, 2011), pp. 351–358.
[23] L. Hsu, W. E. Dietrich, and L. S. Sklar, J. Geophys. Res.: Earth Surf. **119**, 1283 (2014).
[24] R. Kaitna, W. E. Dietrich, and L. Hsu, J. Fluid Mech. **741**, 377 (2014).
[25] I. S. Aranson, F. Malloggi, and E. Clément, Phys. Rev. E **73**, 050302 (2006).
[26] S. Lee, A. Mavromoustaki, G. Urdaneta, K. Huang, and A. L. Bertozzi, Granular Matter **16**, 269 (2014).
[27] N. Murisic, B. Pausader, D. Peschka, and A. L. Bertozzi, J. Fluid Mech. **717**, 203 (2013).
[28] P. Coussot, *Mudflow Rheology and Dynamics* (A. A. Balkema, Rotterdam, 1997), p. 272.
[29] M. J. Woodhouse, A. R. Thornton, C. G. Johnson, B. P. Kokelaar, and J. M. N. T. Gray, J. Fluid Mech. **709**, 543 (2012).
[30] P. Coussot and C. Ancey, Phys. Rev. E **59**, 4445 (1999).
[31] C. Ancey, J. Non-Newtonian Fluid Mech. **142**, 4 (2007).
[32] R. Kaitna, D. Rickenmann, and M. Schatzmann, Acta Geotech. **2**, 71 (2007).
[33] D. Schneider, R. Kaitna, W. Dietrich, L. Hsu, C. Huggel, and B. McArdell, Cold Regions Sci. Technol. **69**, 70 (2011).
[34] R. Kaitna and D. Rickenmann, J. Hydraul. Res. **45**, 797 (2007).
[35] M. Cabrera, D. Gollin, R. Kaitna, and W. Wu, in *Recent Advances in Modeling Landslides and Debris Flows*, edited by W. Wu, Springer Series in Geomechanics and Geoengineering (Springer International Publishing, Berlin, 2014), pp. 57–71.
[36] H. Henein, Bed behavior in rotary cylinders with applications to rotary kilns, Ph.D. thesis, University of British Columbia, 1980.
[37] J. Wu and C. K. Aidun, Int. J. Multiphase Flow **36**, 202 (2010).
[38] H. Henein, J. Brimacombe, and A. Watkinson, Metallurg. Trans. B **14**, 191 (1983).
[39] J. Canny, IEEE Trans. Pattern Analysis and Machine Intelligence, **PAMI-8**, 679 (1986).
[40] O. Švec, J. Skoček, H. Stang, M. R. Geiker, and N. Roussel, J. Non-Newtonian Fluid Mech. **179-180**, 32 (2012).
[41] C. R. Leonardi, D. R. J. Owen, and Y. T. Feng, Eng. Comput. **29**, 392 (2012).
[42] C. R. Leonardi, J. W. S. McCullough, B. D. Jones, and J. R. Williams, Comput. Part. Mech., doi:10.1007/s40571-015-0035-x (2015).
[43] S. Chen and G. D. Doolen, Annu. Rev. Fluid Mech. **30**, 329 (1998).
[44] S. Succi, in *The Lattice Boltzmann Equation for Fluid Dynamics and Beyond* (Oxford University Press, New York, 2001), p. 287.
[45] N. Bicanic, in *Encyclopedia of Computational Mechanics*, edited by E. Stein, R. de Borst, and T. J. R. Hughes (John Wiley & Sons, Chichester, UK, 2007), pp. 311–337.
[46] C. K. Aidun and J. R. Clausen, Annu. Rev. Fluid Mech. **42**, 439 (2010).
[47] A. Leonardi, F. K. Wittel, M. Mendoza, and H. J. Herrmann, Comput. Part. Mech. **1**, 3 (2014).
[48] P. L. Bhatnagar, E. P. Gross, and M. Krook, Phys. Rev. **94**, 511 (1954).
[49] C. Körner, M. Thies, T. Hofmann, N. Thürey, and U. Rüde, J. Stat. Phys. **121**, 179 (2005).
[50] R. Mei, W. Shyy, D. Yu, and L.-S. Luo, J. Comput. Phys. **161**, 680 (2000).

[51] R. Mei, D. Yu, W. Shyy, and L.-S. Luo, Phys. Rev. E **65**, 041203 (2002).
[52] Z.-G. Feng and E. E. Michaelides, J. Comput. Phys. **202**, 20 (2005).
[53] A. Leonardi, F. K. Wittel, M. Mendoza, R. Vetter, and H. J. Herrmann, Computer-Aided Civil and Infrastructure Engineering (2015), doi: 10.1111/mice.12165.
[54] S. K. Kang and Y. A. Hassan, Int. J. Numer. Methods Fluids **66**, 1132 (2011).
[55] Y. Tsuji, T. Tanaka, and T. Ishida, Powder Technol. **71**, 239 (1992).
[56] K.-F. Liu and C.-W. Chang, in *Interpraevent 2010* (International Research Society, 2010), pp. 263–271.
[57] S. Courrech du Pont, P. Gondret, B. Perrin, and M. Rabaud, Phys. Rev. Lett. **90**, 044301 (2003).
[58] C. Cassar, M. Nicolas, and O. Pouliquen, Phys. Fluids **17**, 103301 (2005).
[59] F. Boyer, É. Guazzelli, and O. Pouliquen, Phys. Rev. Lett. **107**, 188301 (2011).
[60] L. Valentik and R. L. Whitmore, Br. J. Appl. Phys. **16**, 1197 (1965).
[61] G. Ovarlez, Q. Barral, and P. Coussot, Nat. Mater. **9**, 115 (2010).
[62] G. Ovarlez, F. Bertrand, P. Coussot, and X. Chateau, J. Non-Newtonian Fluid Mech. **177-178**, 19 (2012).
[63] P. Coussot, J. Non-Newtonian Fluid Mech. **211**, 31 (2014).